



Interpretative and predictive modelling of Joint European Torus collisionality scans

Downloaded from: <https://research.chalmers.se>, 2025-12-04 22:41 UTC

Citation for the original published paper (version of record):

Eriksson, F., Fransson, E., Oberparleiter, M. et al (2019). Interpretative and predictive modelling of Joint European Torus collisionality scans. Plasma Physics and Controlled Fusion, 61(11).
<http://dx.doi.org/10.1088/1361-6587/ab2f45>

N.B. When citing this work, cite the original published paper.

Interpretative and predictive modelling of Joint European Torus collisionality scans

F Eriksson¹ , E Fransson¹ , M Oberparleiter¹ , H Nordman¹, P Strand¹,
A Salmi², T Tala² and JET Contributors³

¹ Chalmers University of Technology, SE-412 96 Göteborg, Sweden

² VTT, FI-02044 Espoo, Finland

E-mail: frida.eriksson@chalmers.se

Received 21 May 2019, revised 27 June 2019

Accepted for publication 4 July 2019

Published 23 September 2019



Abstract

Transport modelling of Joint European Torus (JET) dimensionless collisionality scaling experiments in various operational scenarios is presented. Interpretative simulations at a fixed radial position are combined with predictive JETTO simulations of temperatures and densities, using the TGLF transport model. The model includes electromagnetic effects and collisions as well as $\vec{E} \times \vec{B}$ shear in Miller geometry. Focus is on particle transport and the role of the neutral beam injection (NBI) particle source for the density peaking. The experimental 3-point collisionality scans include L-mode, and H-mode (D and H and higher beta D plasma) plasmas in a total of 12 discharges. Experimental results presented in (Tala *et al* 2017 *44th EPS Conf.*) indicate that for the H-mode scans, the NBI particle source plays an important role for the density peaking, whereas for the L-mode scan, the influence of the particle source is small. In general, both the interpretative and predictive transport simulations support the experimental conclusions on the role of the NBI particle source for the 12 JET discharges.

Keywords: turbulence, ITG, gyro-fluid, modelling, particle transport

(Some figures may appear in colour only in the online journal)

1. Introduction

The main ion density profile in fusion devices is determined by a balance between the particle sources and particle transport which typically includes turbulent diffusive and convective (inward) flows. The resulting density peaking is crucially important for the fusion performance through its impact on the high-Z impurity peaking, the bootstrap current and the fusion power produced. To evaluate the importance of the particle source for the density peaking in present

experiments and improve the extrapolation to ITER and beyond, dedicated dimensionless collisionality scaling experiments have been performed in various scenarios at Joint European Torus (JET) [1]. In the experiments, the collisionality was varied while the other key dimensionless parameters like beta, normalized gyroradius, safety factor, magnetic shear, normalized temperature gradient and Z_{eff} were kept constant within experimental error bars. Using a gas puff modulation technique, developed and optimized in [1], the electron particle transport coefficients were then measured with high resolution diagnostics. The results indicate that for the H-mode scans the neutral beam injection (NBI) particle source plays an important role for the density peaking, whereas for the L-mode scan the influence of the particle source was small and the turbulent pinch was the main contributor to the observed peaking. The H-mode scans also reproduced the strong correlation between collisionality and density peaking observed in multi-machine steady state databases, see [2–4]. This feature is in line with predictions based on the ITG/TE mode turbulence driven particle pinch

³ See the author list of *Overview of the JET preparation for Deuterium-Tritium Operation* Joffrin *et al* to be published in Nuclear Fusion Special issue: overview and summary reports from the 27th Fusion Energy Conference (Ahmedabad, India, 22–27 October 2018).



Original content from this work may be used under the terms of the Creative Commons Attribution 3.0 licence. Any further distribution of this work must maintain attribution to the author(s) and the title of the work, journal citation and DOI.

[5]. We note however, that there is a variation in the observed density peaking at fixed collisionality. While turbulent particle transport driven by drift waves has been investigated theoretically in a number of previous works [6–21], the role of the NBI particle source for the density peaking has recently received more attention [1, 22, 23]. This is the focus of the present work which is based on a unique set of experimental data, including four separate and independent 3-point collisionality scans in (i) high power H-mode with low beta and high magnetic shear, (ii) higher beta H-mode plasma at low magnetic shear, (iii) H-mode plasma in Hydrogen at high magnetic shear and (iv) L-mode with Carbon wall at low collisionality. The large range in collisionality in the different operating scenarios, performed in both Carbon wall and ITER-Like wall (ILW) JET plasmas, and the well match-dimensionless parameters obtained within each scan, makes them ideal for theoretical investigations of the role of the NBI particle source versus the turbulent pinch for density peaking. The 12 discharges are also very well suited for validation studies of transport models. To this end, we perform predictive and interpretative simulations of the JET collisionality scans using the trapped-gyro-Landau-fluid (TGLF) transport model [24, 25] together with the JETTO transport code [26]. The simulation results support the experimental conclusions listed above, and TGLF is found to reproduce the profiles well with averaged RMS errors of 8.4% and 13.4% for the ion and electron temperatures, respectively, and RMS errors below 6% for the density profiles of 11 of the 12 discharges.

The rest of the paper is organized as follows: in section 2 the transport model used to analyze the four collisionality scans is presented. Section 3 introduces the 12 JET discharges that are part of the scans. Section 4 discusses the interpretative and predictive analysis as well as comparison with experiments. Finally, summary and conclusions are given in section 5.

2. Transport model

The TGLF model [24] is the latest generation gyro-Landau-fluid model. Like its predecessors, it includes kinetic effects such as gyro-averaging and Landau damping, though TGLF unifies trapped and passing particles to a single set of equations. Also, it treats electrons, main and fast ions and impurities as well as electron-ion collisions [27] and electromagnetic effects in a shaped Miller geometry [28]. It is a quasi-linear model where a system of moments of the gyrokinetic equation are solved for the linear eigenmodes. The quasi-linear fluxes are calculated for the full spectrum of linear modes, $0.1 < k_\theta \rho_s < 24$ (ρ_s normalized to deuterium). The saturated potential is then modeled to fit a nonlinear gyrokinetic database.

In this paper, the spectral shift saturation model SAT1, presented in [29, 30] is used. TGLF is run predictively using the transport code JETTO as well as stand-alone at a single radial position. The stand-alone simulations use input parameters obtained from JETTO interpretative runs.

3. JET discharges simulated

In this paper, 12 JET discharges are analyzed as part of four separate three point collisionality scans: L-mode with Carbon wall, deuterium, hydrogen and higher beta H-mode in ILW with density profiles given in figure 1. In each scan, the plasma current (I_p), magnetic field on axis (B_t) and the absorbed NBI power (P_{NBI}), presented in table 1, were varied while keeping the dimensionless parameters ρ^* , β , q , \hat{s} , T_i/T_e and a/L_T roughly constant. Here ρ^* is normalized gyroradius, q is the safety factor, \hat{s} the magnetic shear, a is the minor radius and $a/L_T = -a\nabla T/T$ the normalized temperature gradient evaluated with respect to ρ_t (defined as the square root of normalized toroidal flux). The volume averaged density is also similar and the resulting collisionality varies roughly by a factor 5 in each scan.

For these discharges, the electron temperature and density were measured with Thomson scattering and the ion temperature and rotation for the Carbon wall L-mode discharges were measured with charge exchange recombination spectroscopy using the Carbon 6+ line. For the ILW discharges $T_i \approx T_e$ within the measurement accuracy.

Interpretative and predictive simulations are performed for the four collisionality scans including toroidal rotation, collisions and electromagnetic effects. The effect of rotation on density peaking was previously analyzed in [31, 32]. In this paper it is assessed for the low collisionality discharges in each scan where the NBI power is largest. Also how impurities affect the density peaking is analyzed for the low collisionality Carbon wall L-mode discharge (79 811). Fast ions are not included in this work.

4. Results and discussion

In general, the turbulent electron particle flux is given by [2]

$$\Gamma_e = \frac{n_e}{a} \left(D \frac{a}{L_{n_e}} + aV_{\text{th}} + aV_p \right), \quad (1)$$

where n_e is the electron density. The first term inside the bracket is the outward diffusive contribution, given by the diffusivity coefficient D and the normalized electron density gradient ($a/L_{n_e} = -a\nabla n_e/n_e$). The second and third terms represent the convection, known as a ‘pinch’, which can be inward or outward, consisting of a thermal pinch proportional to the electron temperature gradient and a ‘pure’ convection. The density peaking in steady state can be expressed as [33]

$$\frac{a}{L_{n_e}} = -\frac{aV_{\text{tot}}}{D} + \frac{a}{V'|\nabla \rho_t|^2 D n_e} \int_0^{\rho_t} SV'd\rho, \quad (2)$$

where the first term is known as the peaking factor (PF) and the second is the contribution from the source. Here V' is the derivative of the plasma volume and V_{tot} is the total convective velocity. In the interpretative analysis in section 4.1 the density peaking in the absence of sources is determined by finding the density gradient corresponding to zero particle flux, i.e. the PF. The PF is then compared to the

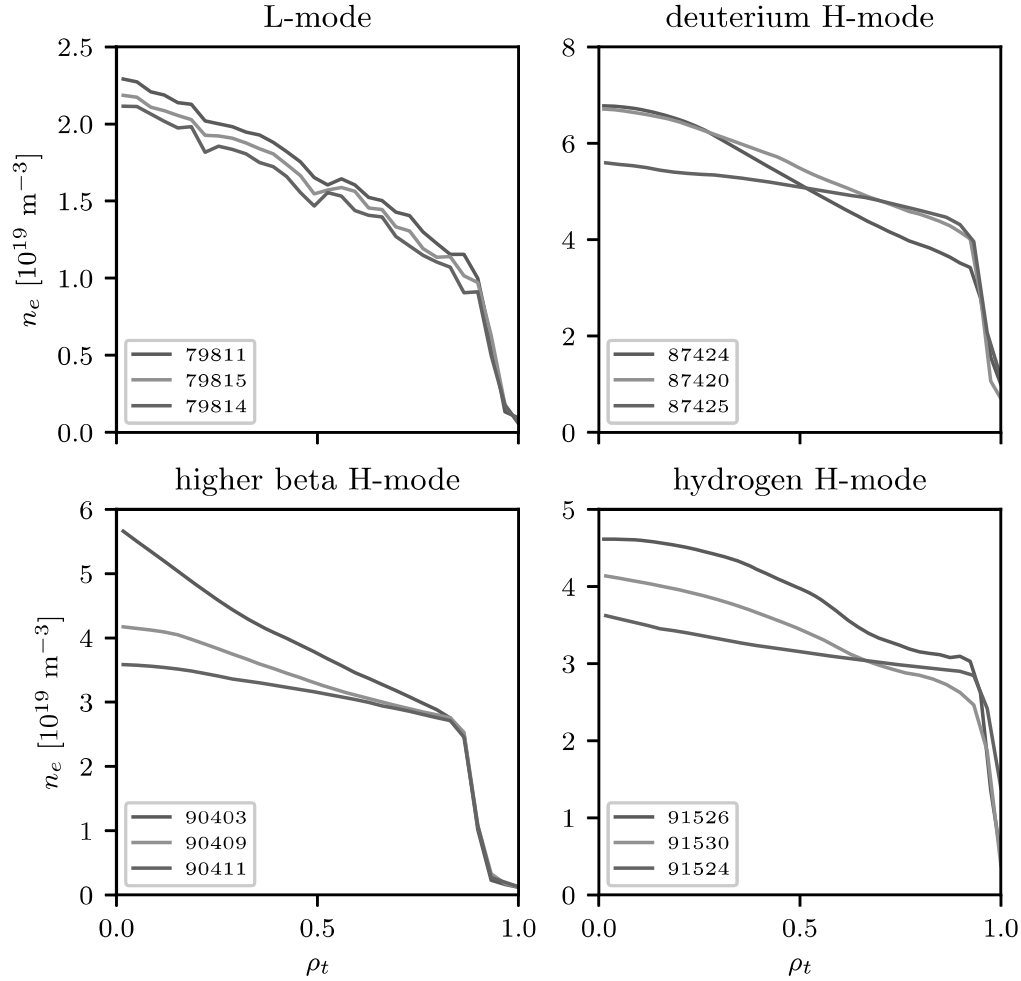


Figure 1. Experimental electron density profiles for the four collisionality scans. Here, ρ_t is the square root of normalized toroidal flux. The location of the separatrix (at $\rho_t = 1$), linked to the equilibrium reconstruction, is slightly off. This causes the density at $\rho_t = 1$ to be too low. Although is not expected to affect the results of the core profiles.

Table 1. Experimental setup for the L-mode, deuterium, higher beta and hydrogen H-mode scans, respectively. Here B_t is the magnetic field at the axis, I_p is the plasma current, P_{NBI} is the absorbed NBI power and ν^* is the experimental collisionality. Only the low collisionality hydrogen H-mode discharge is ICRH heated.

| Discharge | B_t [T] | I_p [MA] | P_{NBI} [MW] | ν^* |
|-----------|-----------|------------|-----------------------|---------|
| 79 811 | 3.3 | 2.0 | 5.8 | 0.05 |
| 79 815 | 2.7 | 1.6 | 3.8 | 0.12 |
| 79 814 | 2.0 | 1.2 | 3.8 | 0.21 |
| 87 424 | 3.4 | 2.5 | 22.4 | 0.1 |
| 87 420 | 2.7 | 2.0 | 12.5 | 0.27 |
| 87 425 | 2.3 | 1.7 | 7.8 | 0.42 |
| 90 403 | 2.0 | 1.7 | 13.3 | 0.074 |
| 90 409 | 1.7 | 1.4 | 10.1 | 0.15 |
| 90 411 | 1.3 | 1.1 | 5.5 | 0.33 |
| 91 526 | 1.7 | 1.7 | 10.0 (2.9 RF) | 0.11 |
| 91 530 | 1.3 | 1.3 | 6.6 | 0.17 |
| 91 524 | 1.0 | 1.0 | 5.1 | 0.55 |

experimentally obtained local density peaking to gauge the importance of the source on the density peaking. Then, in the predictive analysis in section 4.2 a global density peaking is obtained, with and without inclusion of the NBI particle source, and compared with experiments to substantiate the conclusions made in section 4.1. Here, the local PF is also compared to the local peaking of the predicted density profile without sources in order to evaluate the impact of the varying temperature profiles of the predictive simulations. Finally in section 4.3 two error estimates are evaluated for the predictive simulations to quantify the performance of TGLF for these sets of discharges.

4.1. Interpretative simulations

The interpretative analysis is performed at the radial position $\rho_t = 0.6$ with discharge parameters given in table 2. Note that the dimensionless parameters q , \hat{s} and a/L_T match well locally within each scan. The influence of the source on the density peaking was analyzed in [34], with a focus on fast ion effects for the low collisionality L-mode (79 811) and

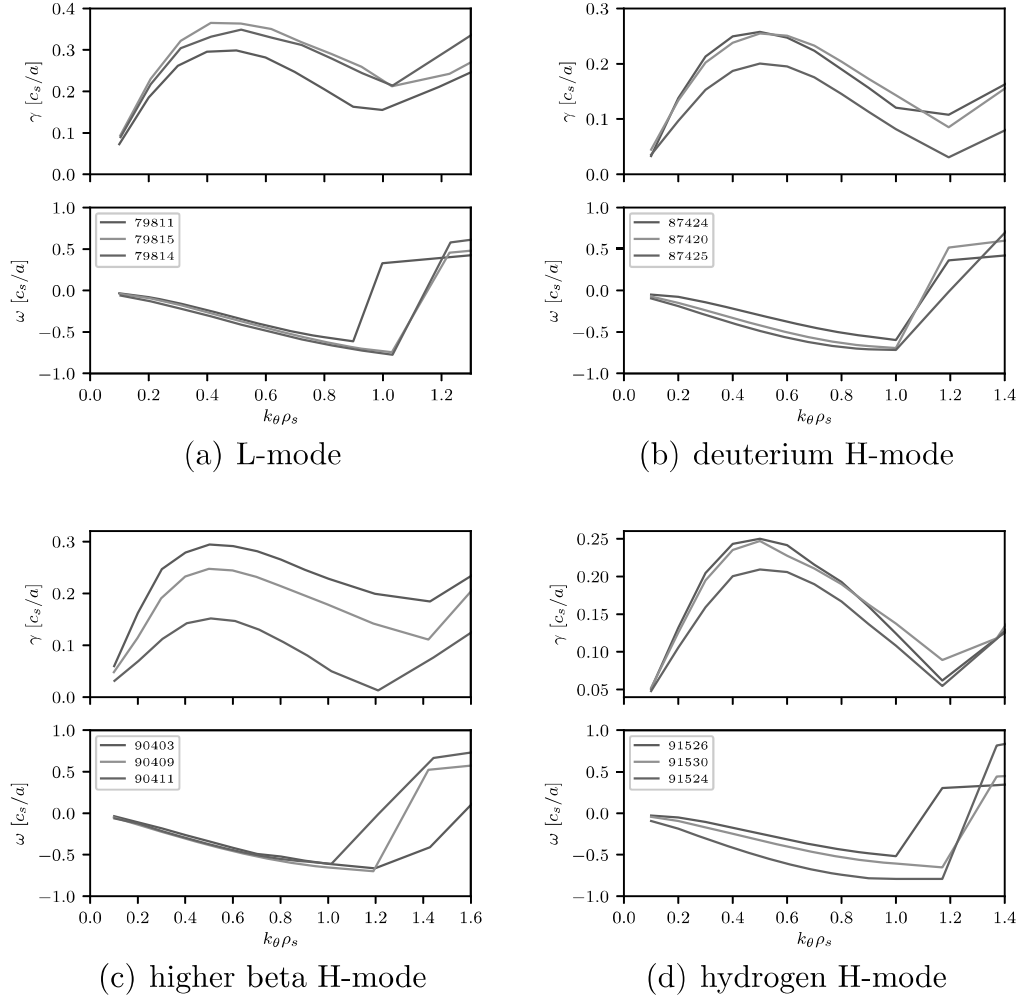
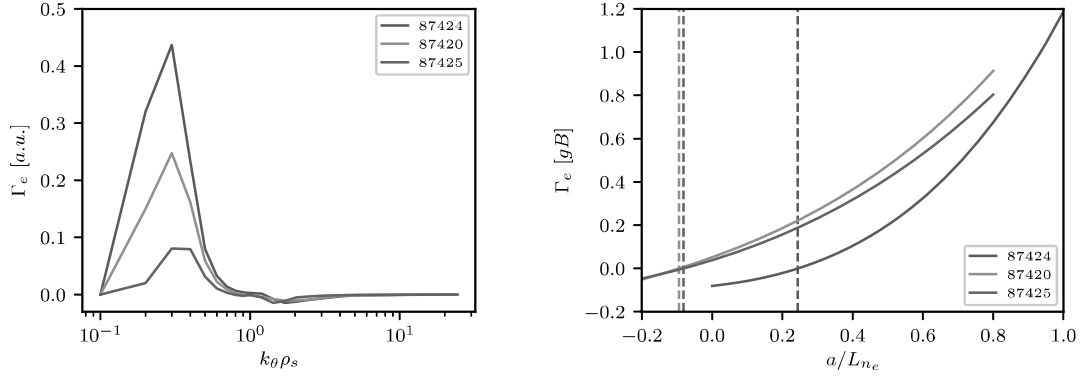


Figure 2. Eigenvalue spectra in c_s/a for all 12 discharges with parameters given in table 2. Here ρ_s and c_s are normalized to deuterium.

Table 2. Discharge parameters at $\rho_t = 0.6$. Here, $a/L_n = -a\nabla n/n$ and $a/L_T = -a\nabla T/T$ are the normalized density and temperature gradients evaluated with respect to ρ_t .

| Discharge | q | \hat{s} | a/L_{T_i} (a/L_{T_e}) | a/L_n | ν_{ei} [c_s/a] | n_e [$10^{19}/\text{m}^3$] | T_e (T_i) [keV] |
|-----------|-------|-----------|-----------------------------|---------|------------------------|--------------------------------|-----------------------|
| 79 811 | 2.554 | 0.935 | 2.328 (2.421) | 0.91 | 0.071 | 1.582 | 1.455 (1.440) |
| 79 815 | 2.436 | 1.125 | 2.843 (2.886) | 1.05 | 0.133 | 1.530 | 1.021 (0.939) |
| 79 814 | 2.360 | 1.251 | 2.907 (3.286) | 0.92 | 0.258 | 1.472 | 0.705 (0.684) |
| 87 424 | 1.950 | 0.859 | 2.155 | 0.96 | 0.137 | 4.702 | 1.699 |
| 87 420 | 1.973 | 0.829 | 2.437 | 0.62 | 0.335 | 5.138 | 1.108 |
| 87 425 | 1.956 | 0.921 | 2.219 | 0.27 | 0.570 | 4.958 | 0.826 |
| 90 403 | 1.918 | 0.627 | 2.512 | 0.83 | 0.096 | 3.446 | 1.685 |
| 90 409 | 1.876 | 0.660 | 2.403 | 0.48 | 0.191 | 3.101 | 1.117 |
| 90 411 | 1.853 | 0.688 | 2.128 | 0.43 | 0.474 | 3.038 | 0.701 |
| 91 526 | 1.499 | 0.683 | 2.117 | 1.14 | 0.155 | 3.658 | 1.373 |
| 91 530 | 1.495 | 0.708 | 2.420 | 0.90 | 0.229 | 3.202 | 1.058 |
| 91 524 | 1.437 | 0.857 | 2.570 | 0.23 | 0.861 | 3.086 | 0.524 |



(a) Electron particle flux spectra as function of wavenumber. (b) Total electron particle flux in gyro-Bohm units as a function of normalized electron density gradient. The vertical dashed lines correspond to zero particle flux (PF_e).

Figure 3. Electron particle flux for the H-mode collisionality scan with discharge parameters given in table 2.

Table 3. Zero flux peaking factor and local density peaking at $\rho_t = 0.6$ in experimental profile and predictive profile w/o NBI particle source for all 12 discharges. (L-mode experimental profiles smoothed).

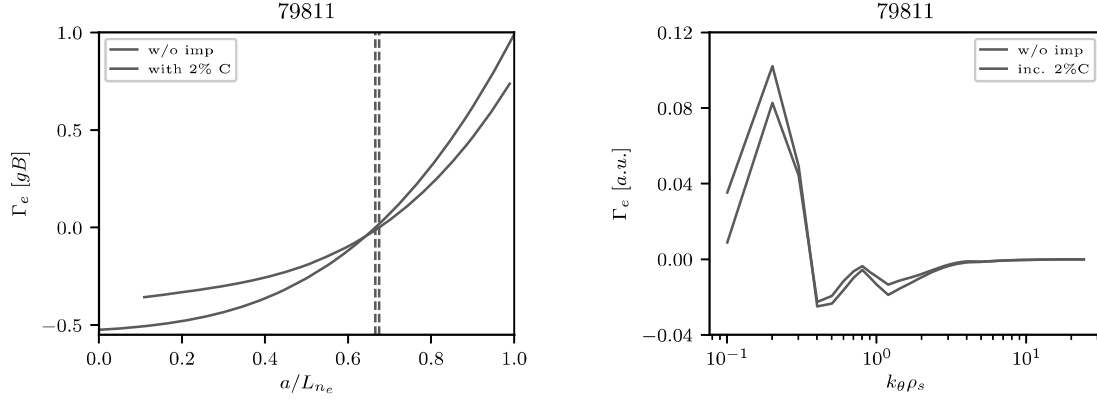
| Discharge | PF_e | a/L_{n_e} exp | a/L_{n_e} predictive |
|-----------|--------|-----------------|------------------------|
| 79 811 | 0.68 | 0.91 | 0.86 |
| 79 815 | 0.66 | 1.05 | 0.76 |
| 79 814 | 0.62 | 0.92 | 0.74 |
| 87 424 | 0.25 | 0.96 | 0.55 |
| 87 420 | -0.1 | 0.62 | 0.36 |
| 87 425 | -0.08 | 0.27 | -0.02 |
| 90 403 | 0.12 | 0.83 | 0.53 |
| 90 409 | 0.19 | 0.48 | 0.36 |
| 90 411 | 0.1 | 0.43 | 0.26 |
| 91 526 | 0.43 | 1.14 | 0.42 |
| 91 530 | 0.33 | 0.90 | 0.38 |
| 91 524 | -0.2 | 0.23 | 0.09 |

deuterium H-mode (87424) discharges. In this section we expand on the results in [34], analyzing all 12 discharges including effects of rotation. For the low collisionality L-mode discharge we also consider the effect of impurities since the L-mode scan was performed in JET Carbon wall with $Z_{\text{eff}} \sim 2$. For the ILW discharges Z_{eff} is significantly lower and the effect of impurities is neglected.

Figure 2 shows the eigenvalue spectrum in ion scales for all 12 discharges. Linear growth rate (γ) and frequency (ω) are given as a function of wavenumber ($k_\theta \rho_s$) for the most dominant unstable mode. The growth rates match well within each scan, as expected with these matched experiments. The largest spread in growth rate is found for the higher beta H-mode scan. A negative frequency indicates that the mode is drifting in the ion diamagnetic direction corresponding to an ITG mode. Electron particle flux spectra for the H-mode discharges are shown in figure 3(a). Here, the magnitude of the particle flux

(Γ_e) is normalized by the number of $k_\theta \rho_s$ -modes in the simulation. A positive Γ_e for the smaller wavenumbers corresponds to an outward flux and the negative Γ_e at $k_\theta \rho_s \approx 1.5$ to an inward flux. This inward flux at intermediate wavenumbers was previously seen in [35]. Most of the contribution to the particle flux occurs at ion scales ($k_\theta \rho_s < 1$) rather than electron scales ($1 < k_\theta \rho_s < 24$). The electron particle flux, given in gyro-Bohm units, as a function of normalized density gradient, is shown in figure 3(b). During the scan in a/L_{n_e} the main ion density gradient is adapted to preserve quasi-neutrality. Note that Γ_e is a sum of the particle flux from multiple wavenumbers between 0.1 and 24. The resulting PFs are illustrated with vertical dashed lines in the figure. PF_e from all 12 discharges are presented in table 3 and compared to the local experimentally obtained peaking at $\rho_t = 0.6$. In addition, a comparison between PF_e and the local gradient of the predictive simulation without sources is shown (see section 4.2 for a discussion of this). Based on the values of PF_e the NBI particle source is responsible for most of the peaking for the H-mode discharges while less so for the L-mode discharges. The higher PF_e for the L-mode discharges is due to differences in local parameters, as shown in [34].

Next we investigate the effect of impurities on the particle flux and density peaking by including 2% Carbon in the low collisionality L-mode discharge (79811). Since the impurities are present in the plasma and have affected the parameters in table 2, the electron density and its gradients are kept fixed while the main ion density is reduced in order to preserve quasi-neutrality. We investigate the effect of a Carbon impurity on the growth rate of the most dominant mode and on the electron particle flux and subsequent PF. The growth rate is reduced which reduces the turbulent fluctuation level. In figure 4 the electron particle flux without and including 2% Carbon is illustrated. Here, the density and temperature gradients of the Carbon ions are set equal to those of the main ions. During the scan in electron density gradient in figure 4(a), the impurity density gradient is kept fixed. The particle flux is reduced by the presence of impurities, though the effect on PF_e



(a) Total electron particle flux in gyro-Bohm units as a function of normalized electron density gradient (b) Electron particle flux as function of normalized electron density wavenumber for $a/L_{n_e} = PF_e$ w/o impurities.

Figure 4. Electron particle flux for discharge 79 811 without and including 2% Carbon.

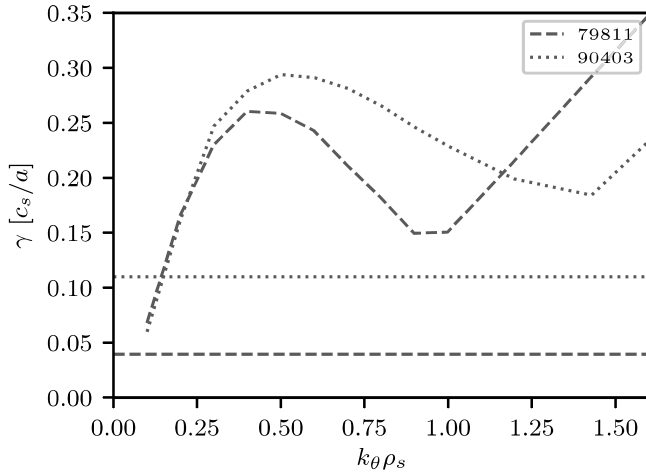


Figure 5. Growth rate spectra overlaid with the $\vec{E} \times \vec{B}$ shear rate for the L-mode discharge (79 811) and higher beta H-mode discharge (90 403).

is marginal due to a reduction of both the outward and inward particle flux, as shown in the particle flux spectra in figure 4(b). These spectra are evaluated at the density gradient corresponding to zero particle flux without impurities.

To evaluate the importance of rotation, the level of $\vec{E} \times \vec{B}$ shear is compared to the growth rate at ion scales for the low collisionality L-mode (79 811) and higher beta H-mode (90 403) discharges and presented in figure 5. Since the volume averaged density is similar within a scan, the influence of rotation is expected to increase with NBI beam power (see table 1). We note that the influence of rotation is expected to be greater for discharge 90 403 than for 79 811.

4.2. Predictive simulations

The predictive simulations were performed with the JETTO transport code together with TGLF for anomalous and NCLASS [36] for the neo-classical transport. The NBI heat and particle source was calculated with the PENCIL code

[37]. The profiles of n_e , T_e and T_i are evolved self-consistently, until steady state is reached (~ 1 s) with boundary conditions at $\rho_r = 0.8$ set by the experimental parameters, while the toroidal rotation and q- profiles are set by the experimental input. Electromagnetic effects and collisions are included and unless otherwise stated so is the effect of $\vec{E} \times \vec{B}$ shear. Also, for the low collisionality L-mode discharge with Carbon wall effects of impurities with radially constant Z_{eff} is analyzed. The impurities are included predictively in the simulations although effect of impurity radiation is neglected.

In figure 6 the experimental and predicted density and temperature profiles are shown for all three discharges in the Carbon wall L-mode collisionality scan without impurities. In the modelling of the low collisionality discharge (79 811), an artificial diffusivity was included for numerical stability in the form of 5% of the Bohm particle diffusivity coefficient [38]. In the top row of figure 6, the experimental density profile is shown in solid black and the predicted one in color. For each of the discharges there are two predictive simulations; the solid line is including the NBI particle source and the dashed is without it. For the low collisionality discharge (79 811) there is a small but noticeable effect of the source on the density peaking while for the other two discharges in the scan (79 815, 79 814), the effect is negligible. The bottom row in figure 6 illustrates the temperature profiles for electrons (solid) and ions (dash-dot). Here the result is shown only when the NBI particle source is included. TGLF reproduces both the electron and ion temperatures well for 79 811 but tends to overpredict the electron temperature for the medium and high collisionality L-mode discharges. This overprediction of T_e is in part due to a lack of impurities and impurity radiation in the simulation. Inclusion of 2% Carbon has a negligible effect on the density peaking of discharge 79 811. Toroidal rotation has a marginal effect on these discharges, see figure 7. This lack of sensitivity to rotation is consistent with the expectation based on figure 5.

Corresponding profiles for the deuterium H-mode collisionality scan are presented in figure 8. For the low and

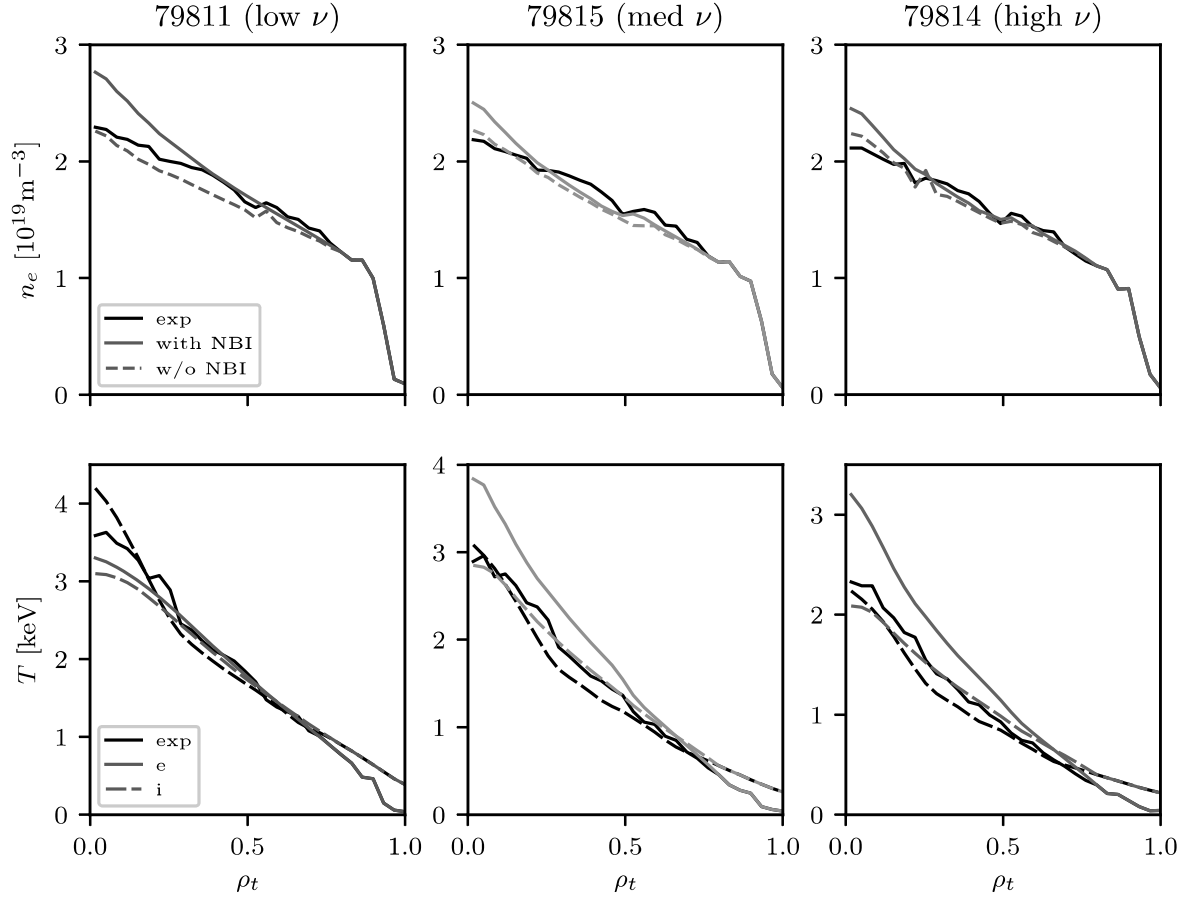


Figure 6. Density (top) and temperature (bottom) profiles for the L-mode collisionality scan given as a function of ρ_t . In black are the experimental profiles and in color the predicted profiles without impurities. The predicted electron density profiles are shown both with (solid lines) and without (dashed lines) the NBI particle source and the temperature profiles are only with particle source (solid lines for electrons and dashed-dotted for ions).

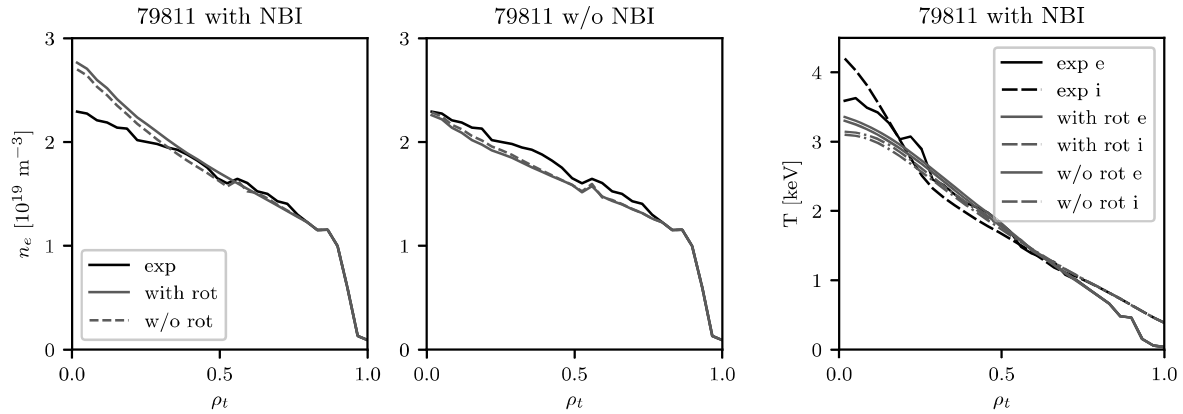


Figure 7. The dependence of the predicted density and temperature profiles on toroidal rotation for the low collisionality L-mode discharge 79811.

medium collisionality discharges (87 424, 87 420) there is a significant contribution of the source to the density peaking. When the source is included, TGLF reproduces the experimental density and temperature profiles well for these two discharges. For the high collisionality discharge (87 425) on the other hand, underprediction of the particle transport close to the edge of the simulation domain ($\rho_t = 0.8$) leads to overprediction of the density for $\rho_t < 0.8$.

The predictive modelling result for the higher beta H-mode collisionality scan is shown in figure 9. Here, the effect of the particle source is significant for the density peaking in the low collisionality discharge (90 403) while being slightly less important for the medium and high collisionality discharges (90 409, 90 411). The temperature predictions match well for these discharges, except that for 90 403 the ion (and electron) temperatures peak up greatly

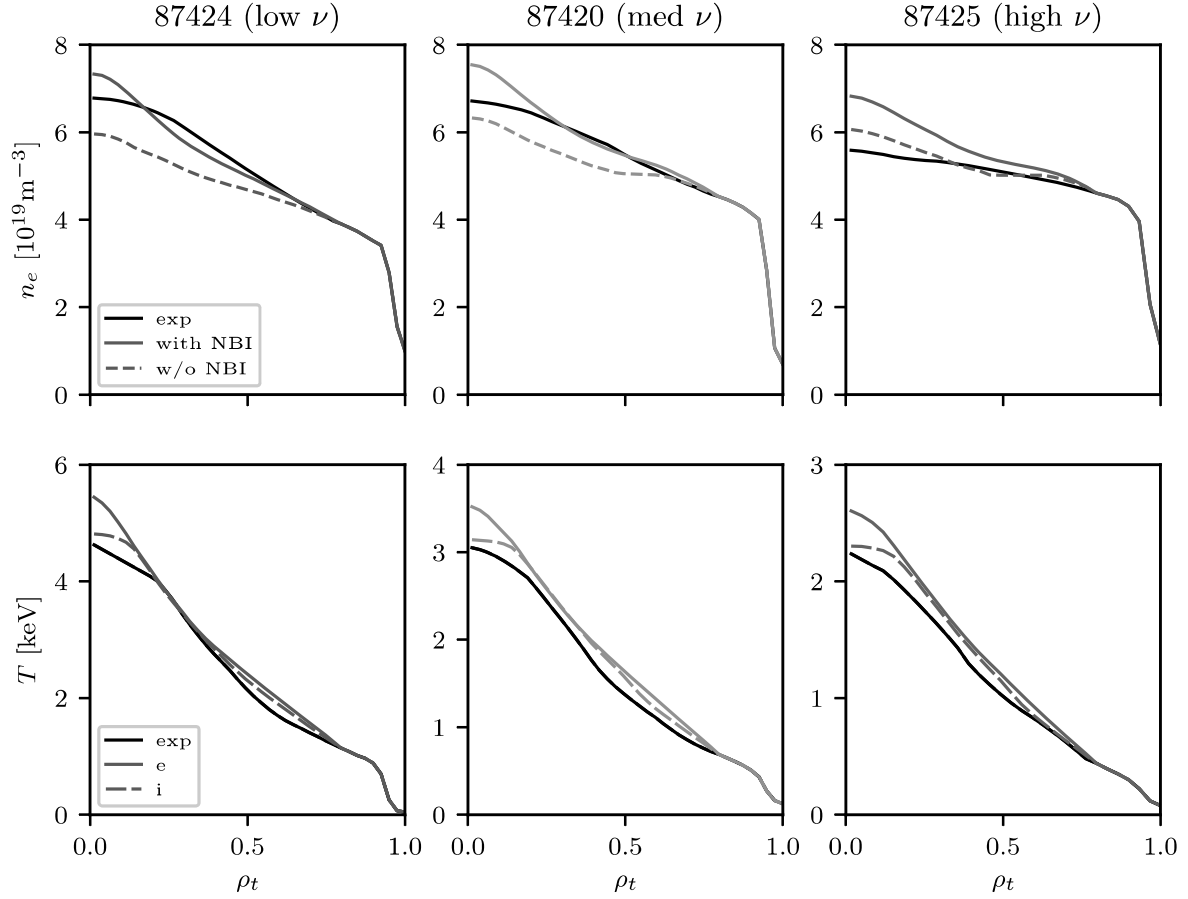


Figure 8. Density (top) and temperature (bottom) profiles for the H-mode collisionality scan. For these ILW discharges the experimental ion and electron temperatures are assumed equal.

inside $\rho_t \approx 0.3$. This overprediction of the temperatures is reduced by the reduction of the $\vec{E} \times \vec{B}$ shear as illustrated in figure 10 where the predicted profiles are shown when the effect of $\vec{E} \times \vec{B}$ shear is included fully and when it is removed. The stabilizing effect of $\vec{E} \times \vec{B}$ shear can be too strong in TGLF, especially close to the centre [39]. Similar to the conclusion for the L-mode discharge 79 811, the sensitivity to rotation for discharge 90 403 is consistent with the interpretative analysis in figure 5.

Finally, for the hydrogen H-mode discharges in figure 11, TGLF predicts the temperatures and density well outside $\rho_t \approx 0.4$ for the low and medium collisionality discharge, however, a barrier at $\rho_t = 0.8$ leads to overprediction of the profiles of the high collisionality discharge (91 524). Here, reducing the effect of $\vec{E} \times \vec{B}$ shear for discharge 91 524 only marginally improves the prediction and it has no effect on the overprediction at the edge of the simulation domain ($\rho_t = 0.8$).

To quantify the effect of the NBI particle source on the density peaking, we compare the ‘global peaking factor’

$$PF_{\text{global}} = \frac{n_e(0.3) - n_e(0.8)}{n_e(0.8)}, \quad (3)$$

with and without the particle source and from the experiment, with the result depicted in figure 12 for all 12 discharges in figures 6, 8, 9 and 11. From figure 12 we also note that the global peaking is independent of collisionality for the L-mode

discharges while the other three scenarios have the expected reduction of peaking as the collisionality increases [2]. The fraction of global peaking coming from the source is given in table 4 for the 12 discharges in figure 12. Based on the values in table 4, the source is responsible for 30%–60% of the density peaking for the H-mode discharges, in line with the experimental conclusions in [1]. For the L-mode discharges on the other hand the impact of the source is weaker, also in agreement with [1].

For these discharges, the predictive simulations underpredicts the effect of the NBI particle source. This is due to overprediction of the temperature profiles in the absence of the particle source given a constant input power. When the temperature gradients are too large the increasing inward thermal pinch lead to an overestimated density gradient. This is illustrated in table 3 where we compare the PFs of section 4.1, calculated using the experimental profiles, with the local peaking in the predictive simulations without particle source. The local density peaking is larger than the PF for all discharges except the low collisionality hydrogen H-mode discharge (91 526). Consequently, the importance of the source tends to be underestimated in the predictive analysis.

4.3. Figures of merit

In order to get a more qualitatively view of how well the predictive simulations performed two statistical errors for the

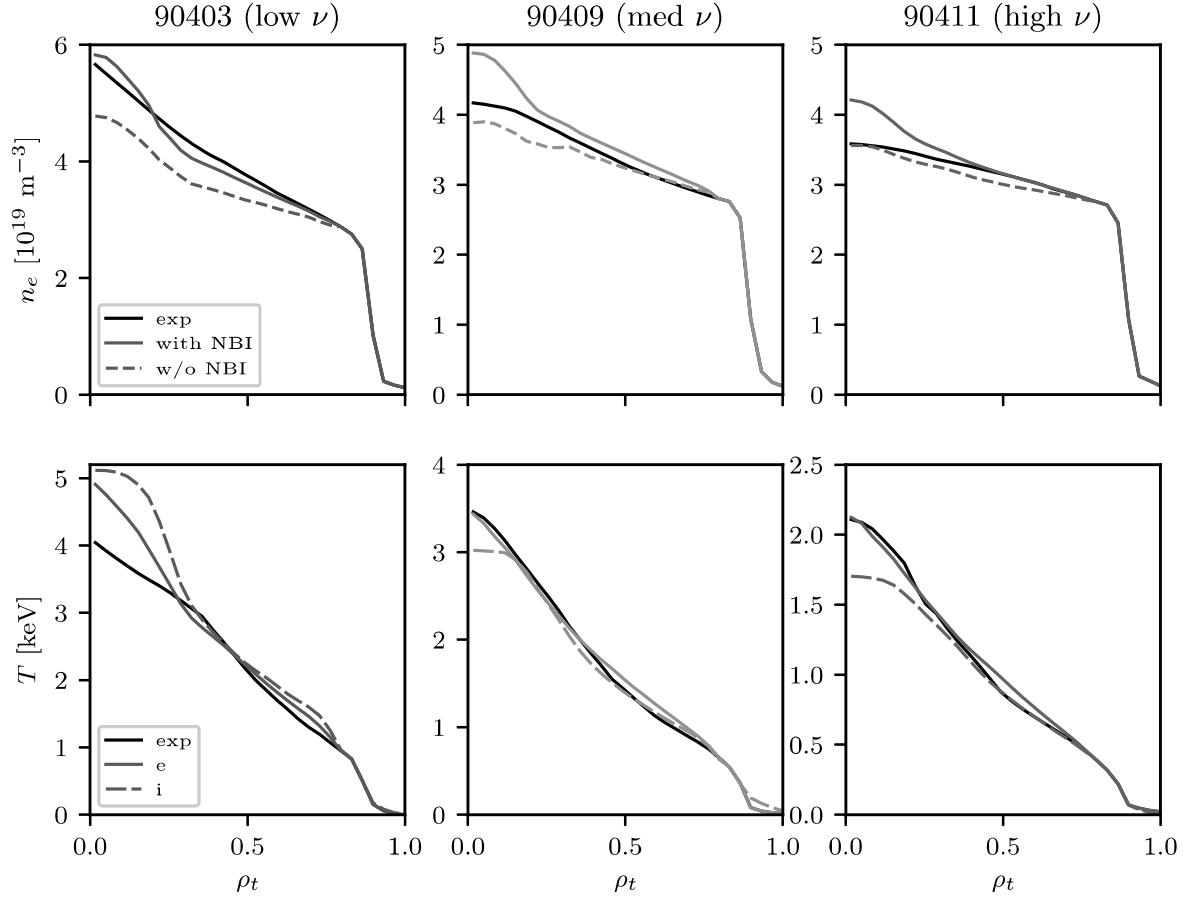


Figure 9. Density (top) and temperature (bottom) profiles for the higher beta H-mode collisionality scan. For these ILW discharges the experimental ion and electron temperatures are assumed equal.

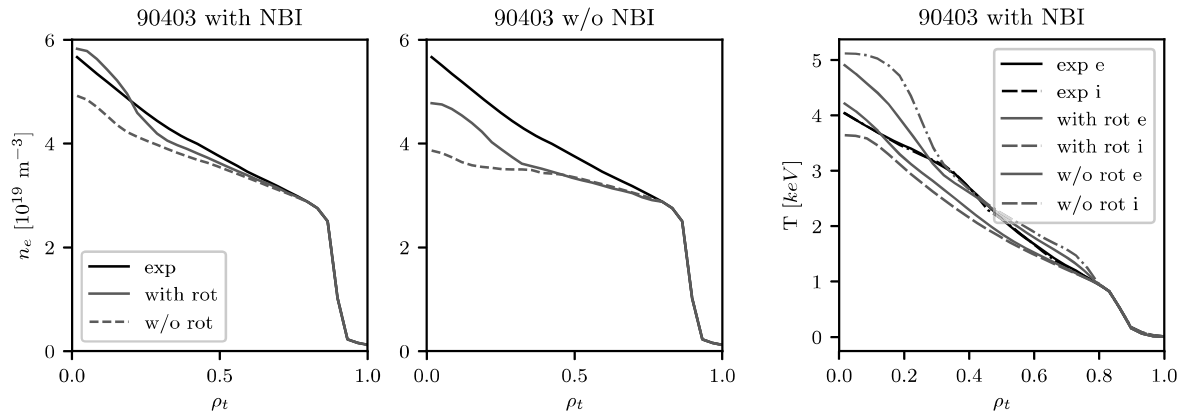


Figure 10. The effect of rotation on the predicted density and temperature profiles for the low collisionality higher beta H-mode discharge 90403.

predictive simulations are used. First, the normalized rms error (σ) is defined by the following equation

$$\sigma = \sqrt{\left\langle \left(\frac{X_{\text{TGLF}} - X_{\text{exp}}}{X_{\text{exp}}} \right)^2 \right\rangle}, \quad (4)$$

where $X_{\text{TGLF}} - X_{\text{exp}}$ is the deviation between the simulated and experimental quantity X corresponding to T_e , T_i or n_e . The brackets indicate averaging between $\rho_t = 0.3$ and $\rho_t = 0.8$. This region is considered since the region inside $\rho_t = 0.3$ is

possibly influenced by effects not included in the simulations. The rms error gives a good indication of the scatter between the experimental and simulated profiles. To determine whether the scatter is due to over- or underprediction the normalized offset

$$f = \left\langle \frac{X_{\text{TGLF}} - X_{\text{exp}}}{X_{\text{exp}}} \right\rangle, \quad (5)$$

is used. The normalized errors and offsets are used because we are interested in the fraction of the error and not the explicit

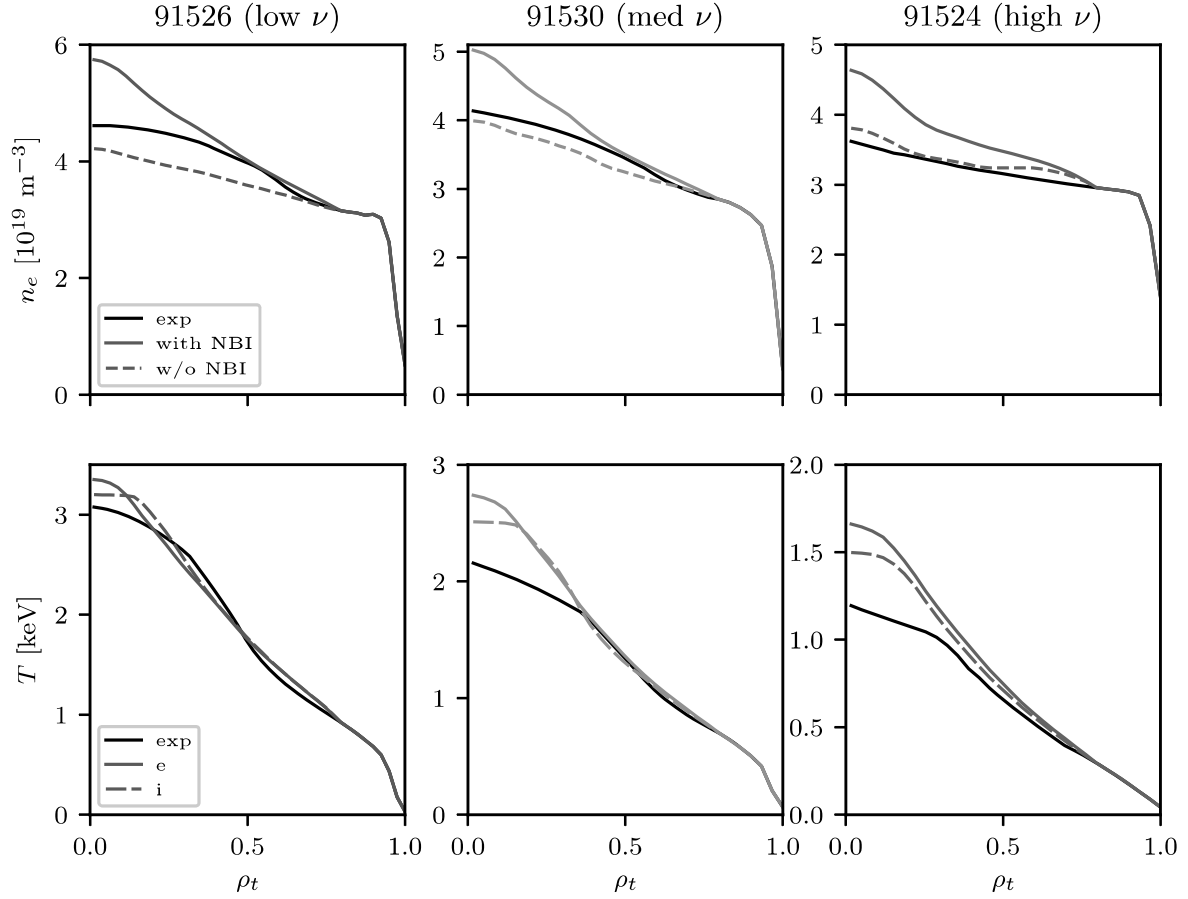


Figure 11. Density (top) and temperature (bottom) profiles for the hydrogen H-mode collisionality scan. For these ILW discharges the experimental ion and electron temperatures are assumed equal.

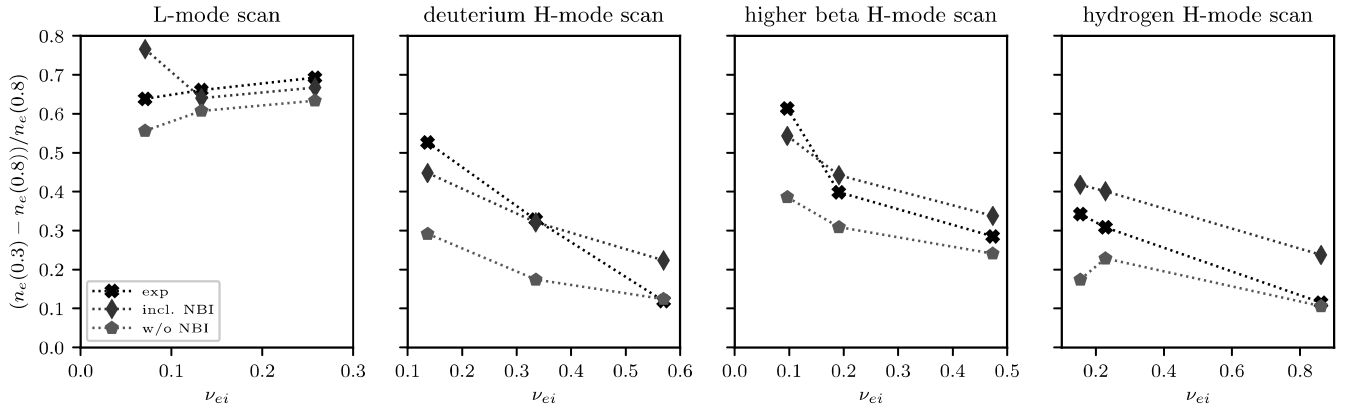


Figure 12. Global peaking of all 12 discharges in figures 6, 8, 9 and 11 with and without NBI particle source compared with the experimental global peaking.

quantity. Note that both of these errors have a bias against overprediction due to the range of our parameters, neither the density nor the temperatures can have a negative value.

These statistical errors show that the temperatures for all of the 12 discharges have been overpredicted by TGLF though the level of overprediction varies between T_e and T_i . Figure 13, which displays the rms error and offset for temperatures with NBI, shows that the electron temperatures have a higher overprediction than the ion temperatures. Averaged over all 12 discharges the rms error for the ion

temperature is 8.4% while it is 13.4% for the electron temperature.

The rms error for the electron density shows that our simulation makes a fine prediction in the middle region of the plasma. All rms errors of the electron density with NBI are lower than 6% except one, 91524 has a 9% error due to the overprediction at $\rho_t = 0.8$. These errors and the corresponding offsets, displayed in figure 14, highlights the underprediction in the density profiles obtained in simulations without the NBI particle source.

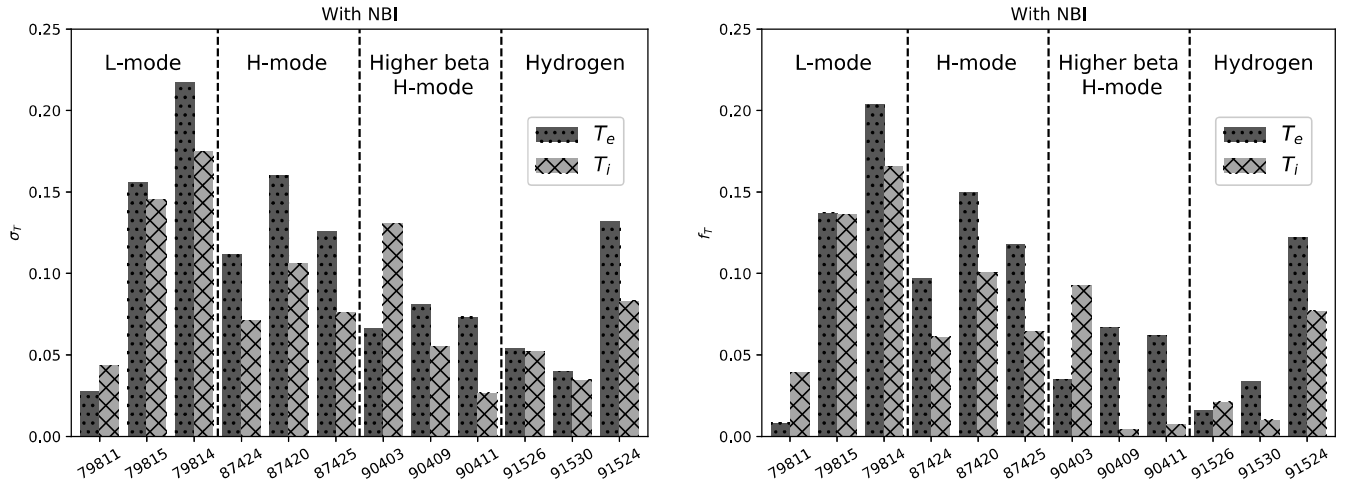


Figure 13. Rms error (left) and offset (right) for the electron and ion temperatures for the predictive simulations with NBI particle source.

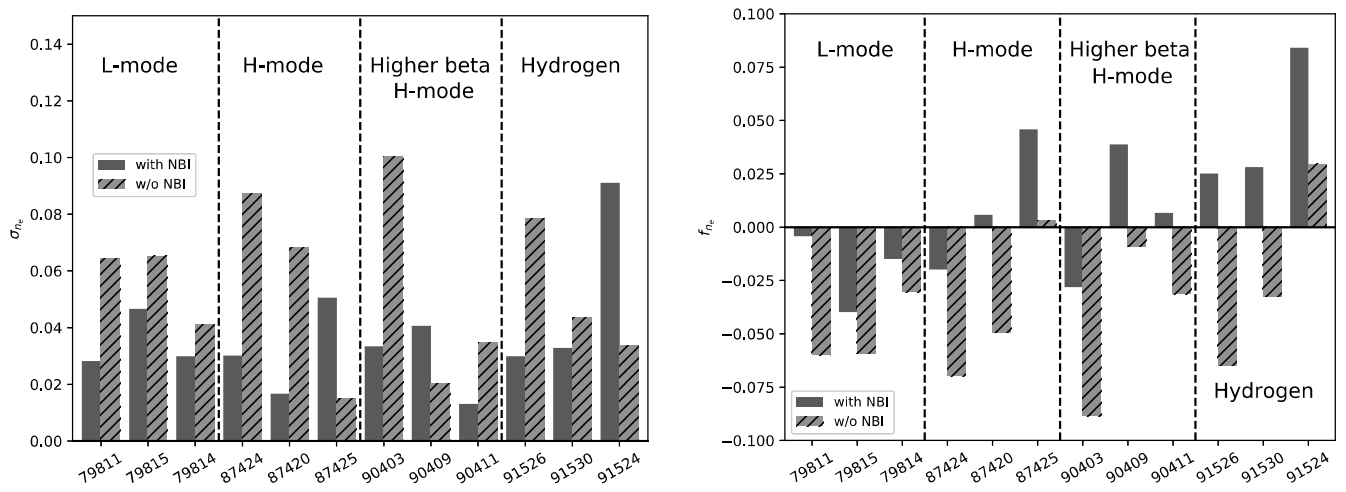


Figure 14. Rms error (left) and offset (right) for the predicted electron density profiles with and without NBI.

5. Summary and conclusions

In the present paper we performed interpretative and predictive modelling of particle transport using the gyro-fluid model TGLF together with the JETTO transport model to evaluate the importance of the NBI particle source on density peaking. The 12 discharges studied are from four dimensionless collisionality scan experiments in various plasma scenarios at JET: Carbon wall L-mode and ILW deuterium, hydrogen and higher beta H-mode plasmas [1]. For the interpretative analysis input parameters were obtained from interpretative JETTO simulations and evaluated at $\rho_t = 0.6$. The zero flux density gradient (peaking factor) was determined for all discharges and compared to the experimentally obtained peaking. At $\rho_t = 0.6$ all 12 discharges are ITG dominated with the main contribution to the density peaking coming from the ion scales. In the predictive modelling, the electron density profile and the electron and ion temperature profiles were evolved until steady state was reached while the rotation and safety factor profiles were taken from the experiment. Predictive simulations were performed with and without the NBI particle source for all 12 discharges including

electromagnetic effects and collisions. Both interpretative and predictive simulations agree that most of the peaking in the L-mode discharges is from the turbulent inward pinch while for the H-mode discharges, the NBI source is significant to the peaking, in agreement with [1]. The influence of impurities was evaluated for the low collisionality L-mode discharge by including 2% Carbon which had a negligible effect on the density peaking. Impurity radiation was neglected in the simulations. Rotation was found to have a small influence on all discharges except the low collisionality higher beta H-mode discharge. For this discharge, TGLF overestimated the stabilization due to $\vec{E} \times \vec{B}$ shear close to the center. In general, TGLF reproduced the profiles well with rms errors below 6% for the density (except 91 524) and an average of 8.4% and 13.4% for the ion and electron temperature, respectively. The overprediction of temperatures is possibly explained by an underprediction of the ion heat transport when the ITG is far from marginal stability [40].

The present paper shows that the TGLF transport model used in predictive and interpretative simulations is able to reproduce well the electron density profiles as well as the experimentally inferred impact of the NBI particle source on

Table 4. Fraction of global density peaking from the NBI particle source based on the values in figure 12.

| Discharge | $\frac{PF_{\text{global lineNBI}} - PF_{\text{global lw/oNBI}}}{PF_{\text{global lineNBI}}} [\%]$ |
|-----------|---------------------------------------------------------------------------------------------------|
| 79 811 | 27 |
| 79 815 | 5 |
| 79 814 | 5 |
| 87 424 | 35 |
| 87 420 | 46 |
| 87 425 | 44 |
| 90 403 | 29 |
| 90 409 | 30 |
| 90 411 | 29 |
| 91 526 | 58 |
| 91 530 | 43 |
| 91 524 | 55 |

the density peaking for these JET collisionality scans. An extension of parameter scans, in particular towards lower collisionality, will be the scope of future experimental work at JET to consolidate ITER predictions with respect to density peaking. In addition, a more comprehensive test of the model, comparing the particle diffusivity (D) and convective velocity (V) separately with the results obtained from the modulation experiments, is left for future work.


Acknowledgments

This work has been carried out within the framework of the EUROfusion Consortium and has received funding from the Euratom research and training programme 2014–2018 and 2019–2020 under grant agreement No 633053. The views and opinions expressed herein do not necessarily reflect those of the European Commission.

ORCID iDs

F Eriksson  <https://orcid.org/0000-0002-2740-7738>

E Fransson  <https://orcid.org/0000-0002-8747-3470>

M Oberparleiter  <https://orcid.org/0000-0001-7282-3020>

References

- [1] Tala T *et al* 2017 *44th EPS Conf. (Belfast, UK)*
- [2] Angioni C *et al* 2009 *Plasma Phys. Control. Fusion* **51** 124017
- [3] Weisen H *et al* 2006 *Plasma Phys. Control. Fusion* **48** A457
- [4] Angioni C *et al* 2009 *Nucl. Fusion* **49** 055013
- [5] Maslov M, Angioni C and Weisen H 2009 *Nucl. Fusion* **49** 075037
- [6] Fröjd M, Liljeström M and Nordman H 1992 *Nucl. Fusion* **32** 419
- [7] Basu R *et al* 2003 *Phys. Plasmas* **10** 2696
- [8] Estrada-Mila C, Candy J and Waltz R W 2005 *Phys. Plasmas* **12** 022305
- [9] Naulin V 2005 *Phys. Rev. E* **71** 015402
- [10] Garzotti L *et al* 2006 *Nucl. Fusion* **46** 994
- [11] Guiret R *et al* 2006 *Plasma Phys. Control. Fusion* **48** B63
- [12] Valović M *et al* 2007 *Nucl. Fusion* **47** 196
- [13] Bourdelle C *et al* 2007 *Phys. Plasmas* **14** 112501
- [14] Dubuit N *et al* 2007 *Phys. Plasmas* **14** 042301
- [15] Nordman H *et al* 2007 *Phys. Plasmas* **14** 052303
- [16] Camenen Y *et al* 2009 *Phys. Plasmas* **16** 012503
- [17] Moradi S *et al* 2009 *Nucl. Fusion* **49** 085007
- [18] Fable E *et al* 2010 *Plasma Phys. Control. Fusion* **52** 015007
- [19] Hein T and Angioni C 2010 *Phys. Plasmas* **17** 012307
- [20] Nordman H *et al* 2011 *Plasma Phys. Control. Fusion* **53** 105005
- [21] Casson F J *et al* 2013 *Nucl. Fusion* **53** 063026
- [22] Tala T *et al* 2019 *Nucl. Fusion* accepted version (<https://doi.org/10.1088/1741-4326/ab4248>)
- [23] Fable E *et al* 2019 *Nucl. Fusion* **59** 076042
- [24] Staerber G M, Kinsey J E and Waltz R E 2005 *Phys. Plasmas* **12** 102508
- [25] Staerber G M, Kinsey J E and Waltz R E 2007 *Phys. Plasmas* **14** 055909
- [26] Cennachi G and Taroni A 1988 *Technical Report JET-IR* (88)03
- [27] Staerber G M and Kinsey J E 2010 *Phys. Plasmas* **17** 122309
- [28] Miller R L *et al* 1998 *Phys. Plasmas* **5** 973–8
- [29] Staerber G M, Howard N T, Candy J and Holland C 2017 *Nucl. Fusion* **57** 066046
- [30] Staerber G M, Candy J, Howard N T and Holland C 2016 *Phys. Plasmas* **23** 062518
- [31] Garcia J *et al* 2014 *Nucl. Fusion* **54** 093010
- [32] Garcia J *et al* 2019 *Plasma Phys. Control. Fusion* **61** 104002
- [33] Baiocchi B *et al* 2015 *Nucl. Fusion* **55** 123001
- [34] Eriksson F *et al* 2019 *Plasma Phys. Control. Fusion* **61** 075008
- [35] Grierson B A *et al* 2018 *Phys. Plasmas* **25** 022509
- [36] Houlberg W A 1997 *Phys. Plasmas* **4** 3230
- [37] Challis C D *et al* 1989 *Nucl. Fusion* **29** 563
- [38] Erba M *et al* 1998 *Nucl. Fusion* **38** 1013
- [39] Mantica P *et al* 2018 *23rd EU-US TTF Meeting (Seville, Spain)*
- [40] Bonanomi N *et al* 2019 *Nucl. Fusion* **59** 096030